Optical Tensor Field Tomography for the Determination of 3D Stress in Photoelastic Materials

D. Schupp

Institut für Meß- und Regelungstechnik, University of Karlsruhe,
Postfach 6980, D-76128 Karlsruhe, Germany
email: schupp@mrt.mach.uni-karlsruhe.de

Abstract *- There are many well-known tomographic methods for the determination of physical quantities in a 2D or 3D space. Most of these quantities are scalar or vectorial. In this paper, a novel method is presented to determine the 3D stress tensor in photoelastic materials by applying optical tensor field tomography. The theory of the projection is described, and the principles of two reconstruction algorithms are explained. The experimental setup is presented, and difficulties in measuring the projections are shown.*

Keywords: tensor field tomography, mechanical stress, integrated photoelasticity, interferometric phase measurement

1. INTRODUCTION

Methods for the determination of stress in transparent materials, which become birefringent in the presence of stress, have been well-known for a long time. However, they are restricted to 2D states of stress or make special assumptions on 3D stress distributions [1]. With the tomographical method presented in this paper, the investigation of arbitrary 3D states of stress is made possible.

In section 2, the interaction between the photoelastic material and the light wave is described. Section 3 explains the principles of the reconstruction algorithms, the limitations of which are shown in section 4. The optical and mechanical setup is presented in section 5, and difficulties arising from the limitations of the reconstruction algorithms are discussed. In section 6, improvements of the algorithms are presented, which consider the poor quality of the object material.

2. INTERACTION BETWEEN THE LIGHT WAVE AND THE PHOTOELASTIC MATERIAL

Many synthetics (e.g. perspex or epoxy) and glass become birefringent in the presence of mechanical stress. The connection between the stress tensor $\underline{\underline{S}}$ and the refractive tensor $\underline{\underline{n}}$ is given by the stress optical equation:

$$\underline{\underline{n}} = n_0 \cdot \underline{\underline{I}} + A \cdot \mathrm{tr}\left(\underline{\underline{S}}\right) \cdot \underline{\underline{I}} + B \cdot \underline{\underline{S}} \,, \tag{1}$$

where $\underline{\underline{I}}$ is the identity tensor, tr(..) is the trace operator, n_0 is the refractive index of the unloaded object, and A and B are photoelastic constants. n_0 only adds a constant phase to the projections, which can be considered during the measurement (see section 5), and can be set to zero in the following derivations. Only deviations of the refractive tensor with respect to $n_0 \underline{\underline{I}}$ will be calculated.

Once the refractive tensor has been determined, the stress tensor can be calculated using eq. (1). This allows us to consider only $\underline{\underline{n}}$ in this paper.

A monochromatic, polarized plane light wave penetrating the object in *z*-direction can be represented by its electrical field vector $\vec{E}(\vec{x}) = \left[E_x, E_y\right]^{\mathrm{T}}$, according to Jones' formalism [9]. The following differential equation describes the interaction of the wave with the material:

$$\frac{\partial \vec{E}(\vec{x})}{\partial z} = -\mathrm{j}k\underline{\underline{n}}^{\perp}(\vec{x}) \cdot \vec{E}(\vec{x}) \,, \tag{2}$$

where k is the wave number and $\underline{\underline{n}}^{\perp}$ is the projection of the refractive tensor in the direction of the light ray:

$$\underline{\underline{n}}^{\perp} = \begin{bmatrix} n_{xx} & n_{xy} \\ n_{xy} & n_{yy} \end{bmatrix} . \tag{3}$$

The transmitted light $\vec{E}_L(x,y)$ is the solution of eq. (2) at the exit $z = L$ of the object:

$$\vec{E}_L(x,y) = \underline{\underline{\Phi}}_0^L(x,y)\left\{\underline{\underline{n}}^{\perp}\right\} \cdot \vec{E}_0(x,y) \,, \tag{4}$$

where $\vec{E}_0(x,y)$ is the electrical field vector of the incident light at $z=0$. $\underline{\underline{\Phi}}_0^L(x,y)\{\underline{\underline{n}}^\perp\}$ is the so-called transition matrix of the object along the light ray (see figure 1), which is also known as Jones matrix. It consists of 4 complex components and describes the *integral* effect of the object on the light ray:

$$\underline{\underline{\Phi}}_0^L(x,y)\{\underline{\underline{n}}^\perp\}=\begin{bmatrix}\phi_{xx}(x,y) & \phi_{xy}(x,y)\\ \phi_{yx}(x,y) & \phi_{yy}(x,y)\end{bmatrix}. \qquad (5)$$

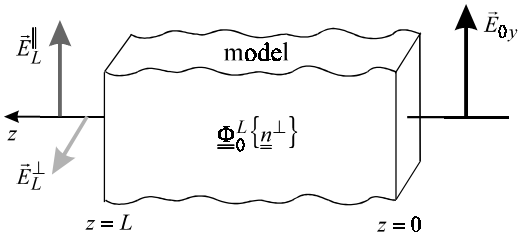

Figure 1: Determination of two components of the transition matrix.

For a special choice of the polarization of the incident light in y-direction, $\vec{E}_0=\vec{E}_{0y}=[0,1]^{\mathrm{T}}\cdot\hat{E}$, and by introducing a polarizer behind the object, which is oriented parallel or perpendicular to the plane of vibration of the incident light, one extracts two components of the transmitted light:

$$\vec{E}_L^{\parallel}=\begin{bmatrix}0\\ \phi_{yy}\end{bmatrix}\cdot\hat{E} \quad\text{and}\quad \vec{E}_L^{\perp}=\begin{bmatrix}\phi_{xy}\\ 0\end{bmatrix}\cdot\hat{E}\ . \qquad (6)$$

By measuring magnitude and phase of $\vec{E}_L^{\parallel}$ and $\vec{E}_L^{\perp}$, and the amplitude $\hat{E}$, two components of the transition matrix, ϕ_{yy} and ϕ_{xy}, can be calculated. They serve as input for the reconstruction algorithms explained in section 3.

As mentioned above, the transition matrix is a measure for the integral effect of the object on the light along the whole path through it [7]. In the general case, where the principal directions of $\underline{\underline{n}}^\perp$ are not constant along the light ray, $\underline{\underline{\Phi}}_0^L\{\underline{\underline{n}}^\perp\}$ has to be calculated by dividing the path through the object into infinitesimal small pieces of length Δz_i; see figure 2. For each one, a transition matrix can be calculated. $\underline{\underline{\Phi}}_0^L\{\underline{\underline{n}}^\perp\}$ then reads:

$$\underline{\underline{\Phi}}_0^L\{\underline{\underline{n}}^\perp\}=\lim_{m\to\infty}\{\underline{\underline{\Phi}}_{z_{m-1}}^{L}\cdot\underline{\underline{\Phi}}_{z_{m-2}}^{z_{m-1}}\cdot\ldots\cdot\underline{\underline{\Phi}}_0^{z_1}\} \qquad (7)$$

with

$$\underline{\underline{\Phi}}_{z_{i-1}}^{z_i}\{\underline{\underline{n}}^\perp\}=\mathrm{e}^{-\mathrm{j}k\underline{\underline{n}}^\perp(z_i)\Delta z_i}. \qquad (8)$$

For a finite discretization, eq. (7) is only an approximation.

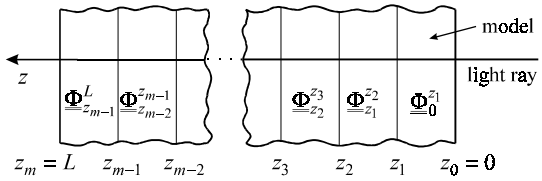

Figure 2: Successive calculation of the transition matrix.

Beside eq. (7), an implicit expression for the transition matrix can be deduced:

$$\underline{\underline{\Phi}}_0^L\{\underline{\underline{n}}^\perp\}=\underbrace{\underline{\underline{I}}-\mathrm{j}k\int_0^L\underline{\underline{n}}^\perp(z)\,\mathrm{d}z}_{\text{linear part}}\underbrace{-k^2\int_0^L\underline{\underline{n}}^\perp(z)\int_0^z\underline{\underline{n}}^\perp(z')\underline{\underline{\Phi}}_0^{z'}\{\underline{\underline{n}}^\perp\}\,\mathrm{d}z'\,\mathrm{d}z.}_{\text{non-linear part}} \qquad (9)$$

3. TOMOGRAPHIC ALGORITHMS

As shown in the previous section, two components of the transition matrix can be determined experimentally by magnitude and phase, which serve as input data for the reconstruction. They must be measured for many orientations of the object with respect to the illuminating light wave. To ease the derivation of the algorithms, the object is rotated around three axes, which are orthogonal to each other. The angles of rotation are equidistant.

With this measurement scheme, one obtains 6 independent 2D data sets (3 axes and 2 components) depending additionally on the projection angle. This is sufficient to reconstruct the 3D stress tensor with its 6 independent components.

3.1 Analytical reconstruction algorithm

Neglecting the non-linear part in eq. (9), the linear approximation of $\underline{\underline{\Phi}}_0^L\{\underline{\underline{n}}^\perp\}$ is a line integral:

$$\underline{\underline{\Phi}}_0^L\{\underline{\underline{n}}^\perp\}=\underline{\underline{I}}-\mathrm{j}k\int_0^L\underline{\underline{n}}^\perp(z)\,\mathrm{d}z\,, \qquad (10)$$

resulting in two projections according to the measurement scheme introduced above:

$$p^{\parallel}(x,y)=\frac{1-\phi_{yy}}{\mathrm{j}k}\ \text{and}\ p^{\perp}(x,y)=\frac{-\phi_{xy}}{\mathrm{j}k}. \qquad (11)$$

For the light propagating in the z-direction, this corresponds to line integrals over n_{yy} or n_{xy}, respectively. For an arbitrary orientation of the object, n_{yy} and n_{xy} must be replaced by two components of the projection of $\underline{\underline{n}}$ in the direction of the light ray [7].

With known projections $p^{\parallel}$ and $p^{\perp}$ for many orientations, an algorithm can be formulated to reconstruct $\underline{\underline{n}}(\vec{x})$ by using the *projection slice theorem* [4]; see figure 3.

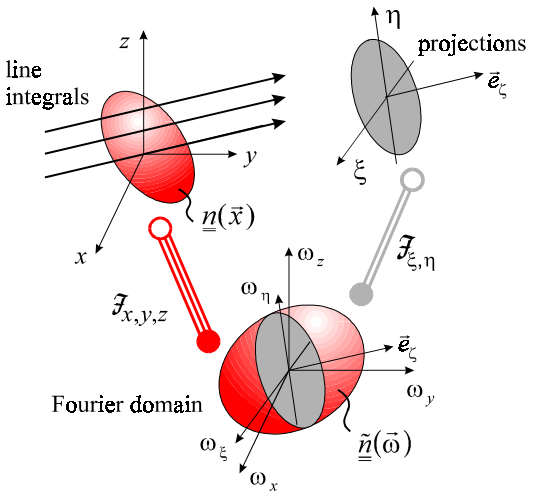

Figure 3: 3D projection slice theorem.

The 2D Fourier transform of the projections is taken with respect to their lateral parameters ξ and η. It corresponds to a central slice through the 3D Fourier transform of the refractive tensor $\underline{\underline{\tilde{n}}}(\vec{\omega}) = F_{x,y,z}\{\underline{\underline{n}}(\vec{x})\}$. By generating projections with different orientations, the Fourier domain is filled up with slices. To calculate $\underline{\underline{n}}(\vec{x})$ by its Fourier transform, a system of linear algebraic equations has to be solved.

It would be beyond the scope of this paper to present the solution in detail. It is only shown, which projection data are needed to calculate the components of the refractive tensor:

$$n_{\alpha\alpha}(\vec{x}) = f\left(p_{\alpha}^{\parallel}(\xi,\eta)\right), \tag{12}$$

$$n_{\alpha\beta}(\vec{x}) = g\left(p_x^{\perp}(\xi,\eta), p_y^{\perp}(\xi,\eta), p_z^{\perp}(\xi,\eta)\right), \tag{13}$$

with $\alpha,\beta = x,y,z;\ \alpha \neq \beta$.

That is, for the computation of the elements in the main diagonal of $\underline{\underline{n}}$, projection data are used resulting from a rotation of the object around the corresponding axis, e.g. the x-axis for the calculation of n_{xx}, and with the polarizer being parallel to the plane of vibration of the incident light. For the determination of the other elements of $\underline{\underline{n}}$, all projections are needed with the polarizer being oriented perpendicular to the illuminating light. Projection data are used from the rotation around all three axis.

With eqs. (12) and (13), an operator P_{lin}^{-1} can be defined for the reconstruction of the refractive tensor in the case of the linearized projection (10), which is used to solve the non-linear problem *iteratively:*

$$\underline{\underline{n}}(\vec{x}) = P_{\text{lin}}^{-1}\left\{\frac{1}{\mathrm{j}k}\left(\underline{\underline{I}} - \underline{\underline{\Phi}}_{0}^{L}\right) + \mathrm{j}k\int_0^L \underline{\underline{n}}^{\perp}(z)\int_0^z \underline{\underline{n}}^{\perp}(z')\underline{\underline{\Phi}}_{0}^{z'}\left\{\underline{\underline{n}}^{\perp}\right\}\mathrm{d}z'\,\mathrm{d}z\right\}. \tag{14}$$

In a first step, $\underline{\underline{n}}(\vec{x})$ is calculated neglecting the double integral. On the basis of this estimate, the double integral is calculated, where $\underline{\underline{\Phi}}_{0}^{z'}$ are projection data for a certain penetration corresponding to z'.

The operator P_{lin}^{-1} only needs two components of the measured transition matrix $\underline{\underline{\Phi}}_{0}^{L}$, see eqs. (12) and (13). Thus, only two components of the correction term of the iteration – the double integral – are necessary.

3.2 Algebraic Reconstruction Technique

In connection with scalar tomography, e.g. X-ray tomography, the *A*lgebraic *R*econstruction *T*echnique (ART) is well-known [4]. Its main difference to analytical methods is the fact that the projection is represented as a discrete operator. The 3D space to be investigated is partitioned into many voxels, which should be cubes to ease the calculations. The aim is to calculate $\underline{\underline{n}}_i$ in the centre of each voxel. $\underline{\underline{n}}_i$ is assumed to be constant inside each voxel.

The projections are computed by calculating the transition matrix for each voxel using eq. (8) while taking into account the length of a light ray inside the voxel. The total effect of the object on the light ray is then given by eq. (7).

In scalar tomography, the set of projections builds a linear system of equations. In the case of tensor tomography discussed here, the projections depend *non-linearly* on the refractive tensors $\underline{\underline{n}}_i$. Therefore, the projections can *not* be described *directly* by a linear system of equations. The problem must be linearized first.

To calculate a solution for the real non-linear problem, the values for the refractive tensor must be calculated iteratively:

$$\underline{\underline{n}}^{(k+1)} = \underline{\underline{n}}^{(k)} + \Delta\underline{\underline{n}} \qquad \text{(outer iteration)}, \tag{15}$$

where $\Delta\underline{\underline{n}}$ is the refractive tensor resulting from the linearized problem.

For the determination of $\Delta\underline{\underline{n}}$, a linear system of equations can be formulated:

$$\underline{\underline{A}}\left\{\underline{\underline{n}}^{(k+1)}\right\}\cdot\Delta\vec{n} = \vec{M} - \vec{P}\left\{\underline{\underline{n}}^{(k+1)}\right\}, \tag{16}$$

where $\underline{\underline{A}}\left\{\underline{\underline{n}}^{(k+1)}\right\}$ is the system matrix, which describes the *linearized* effect of each component of the refractive tensor in all voxels on each projection, with varying direction of the projection and orientation of the polarizer. The system matrix is calculated before each iterative computation of $\Delta\vec{n}$ using the result $\underline{\underline{n}}^{(k+1)}$ of the last outer iteration; see eq. (15). $\Delta\vec{n}$ consists of the 6 independent components of the refractive tensors in all voxels, which are reordered to build a vector. The vector $\vec{M} - \vec{P}\left\{\underline{\underline{n}}^{(k+1)}\right\}$ is the difference of the measured projections $\vec{M}$ and the projections $\vec{P}\left\{\underline{\underline{n}}^{(k+1)}\right\}$, which are computed on the basis of the result $\underline{\underline{n}}^{(k+1)}$ of the preceding iteration in eq. (15).

Because usually the number of projections is smaller than the number of components of $\Delta\vec{n}$, the system (16) can not be solved by inverting the system matrix, but is solved iteratively by applying ART [4].

4. RECONSTRUCTION QUALITY

In both algorithms shown in the preceding section, a linearization of the projections has been performed. In addition, the calculation is done iteratively. For this reason, the range of convergence should be expected to be limited.

To study the reconstruction quality and to determine the limits of the reconstruction algorithms, many different reconstructions have been done on the basis of simulated projection data. For this purpose, arbitrary 3D states of stress have been used. The reconstruction area has been a cube with an edge length of 30 mm. This corresponds to the dimensions of the objects which can be investigated experimentally.

The numerical expense and the amount of data of the tomographic reconstruction are very high. Thus, the chosen 2D or 3D grids were not very dense: 32 points are used in each direction.

To visualize the reconstruction quality, results are shown in figure 4 that correspond to a cylinder built of perspex, which has been exposed to torsional stress. The results for two different twisting moments are shown for both reconstruction algorithms together with the original distribution in a slice perpendicular to the cylinder axis. Exemplarily, one component n_{yz} of the refractive tensor is depicted with the Z-axis being the axis of the cylinder.

As a result of a great number of simulations it can be summarized that the reconstruction quality is good for both algorithms in the case of low stress. However, the algorithms diverge when the stress exceeds a certain limit. This limit is reached when the projections show phase shifts of more than π, corresponding to a difference in the optical path length of more than half a wavelength $\frac{\lambda}{2}$ of the illuminating light.

The reason for the divergence presumably is the ambiguity of the projections for phase shifts of more than π, because these complex quantities contain the phase modulo 2π.

Taking into account the absolute values of the phase by the reconstruction algorithms would enlarge the area of application to higher stresses, but unfortunately an *absolute phase is not defined* for integrated (3D) photoelasticity [2].

The restrictions to the objects to be tested with the method described here and the requirements concerning the quality of the measurement process are discussed in the following section.

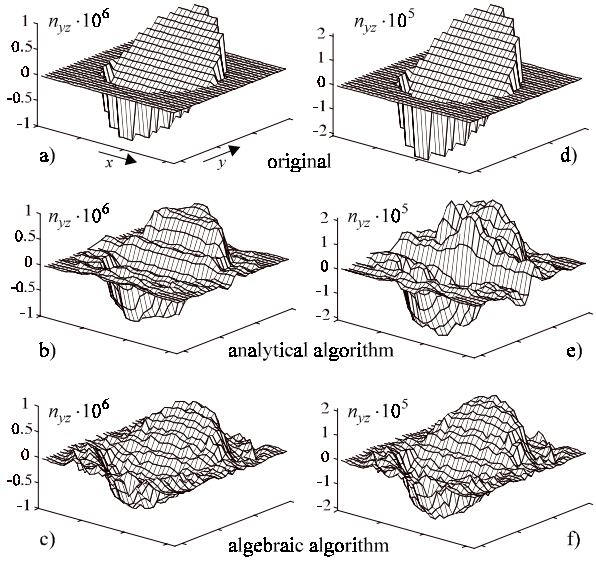

Figure 4: Results of reconstructions with simulated projections: cylinder, perspex, diameter 20 mm, length 10 mm. Twisting moments: a)-c) M=0.4 Nm, d)-f) M=10 Nm.

5. EXPERIMENTAL REALIZATION

5.1 Principle

To acquire the projection data, the test object is illuminated with a monochromatic polarized plane light wave from different directions. For each orientation, two components of the transition matrix,

$$\phi^{\parallel} = \hat{\phi}^{\parallel} \cdot \mathrm{e}^{-\mathrm{j}\varphi^{\parallel}} \quad \text{and} \quad \phi^{\perp} = \hat{\phi}^{\perp} \cdot \mathrm{e}^{-\mathrm{j}\varphi^{\perp}}, \qquad (17)$$

have to be determined by magnitude and phase. Thus, a polarizer is installed behind the object, which can be oriented parallel or perpendicular to the plane of vibration of the incident light.

The phase values $\varphi^{\parallel}$ and $\varphi^{\perp}$ are determined with an interferometer. The object is placed in a cuvette filled with an immersion fluid having exactly the same refractive index as the object material without load. With the immersion fluid, arbitrary shaped objects can be examined, and the refractive

index n_0 of the object has not to be considered, as it was postulated in section 2.

Since the phase measured with an interferometer with imperfect optics is not zero for the whole field of view, a reference phase measurement has to be done without an object being in the laser beam. The phase shift introduced by the object can then be calculated as the difference of the phase with the object $\varphi_{\mathrm{M}}^{\parallel/\perp}$ and the reference phase $\varphi_0^{\parallel/\perp}$ for both states of polarization:

$$\varphi^{\parallel/\perp} = \varphi_{\mathrm{M}}^{\parallel/\perp} - \varphi_0^{\parallel/\perp}. \tag{18}$$

The magnitude of the two components of the transition matrix is determined by measuring the intensity $I_{\mathrm{M}}^{\parallel/\perp}$ with the object and the intensity of the illuminating light wave. The latter is equivalent to the intensity $I_0^{\parallel}$ measured without object and the polarizer being parallel to the plane of vibration of the incident light. The magnitudes then read:

$$\hat{\phi}^{\parallel/\perp} = \sqrt{\frac{I_{\mathrm{M}}^{\parallel/\perp}}{I_0^{\parallel}}}. \tag{19}$$

5.2 Setup

In figure 5 the experimental setup is shown schematically. It is a Mach-Zehnder interferometer, which is used for the phase measurement. To determine the magnitude, the reference beam of the interferometer is blocked, and the setup works as a conventional polariscope.

The illuminating HeNe-laser is expanded to match the dimensions of the object, and is spatially filtered. If the shutter is in position (1), the light passes through the object, which is in the cuvette. After being reflected by the beam splitter BS2, it traverses the rotatable polarizer. The object is then focussed on the CCD-camera by a lens system. The video signal of the camera is digitized by a frame grabber. In this configuration, the intensity is measured as with a conventional polariscope, which is needed for the determination of the magnitude.

For the phase measurement, a reference beam is needed, which is available if the shutter is in position (2). The plane of vibration of the beam reflected at beam splitter BS1 is rotated by 45° by the half-wave plate. Thus, for both orientations of the polarizer a part of the reference beam exists, which builds an interference pattern on the CCD chip together with the beam traversing the object.

To obtain the interference phase, a phase stepping technique is applied, see section 5.3. The additional phase shift between the object and the reference beam is generated by a piezo-driven mirror.

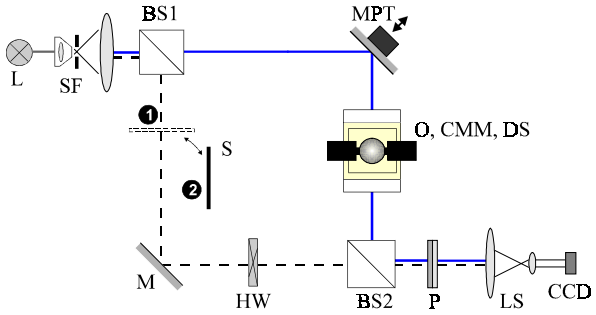

Figure 5: Experimental setup (schematic). L: laser, SF: spatial filter, BS: beam splitter, O: object, CMM: cuvette with mini-manipulator, DS: dosing system for immersion fluid and stirrer, S: shutter, HW: half-wave plate, P: polarizer, LS: lens system, CCD: camera.

The orientation of the object with respect to the light wave has to be changed during the measurement process. This is done automatically by a mechanical, step motor driven mini-manipulator, which stepwise rotates the object inside the immersion fluid around three orthogonal axes.

The immersion fluid is mixed automatically of two components to match exactly the refractive index of the object. The micro dosing of the fluid is controlled by the PC. During the measurement the fluid is stirred continuously.

Because of the large number of images (several hundreds) taken for one complete data acquisition cycle and the great sensitivity of the interferometric phase measurement, the rotation of the polarizer, the positioning of the shutter, and the shifting of the mirror must be done automatically, too.

5.3 Post processing of the image data

From the digitized images the relevant area is cut out, which has to be post processed.

As a result of imperfection of the optics, the images on the CCD camera are distorted. This distortion is corrected using standard algorithms known from computer vision [10]. Afterwards, the high resolution images ($512 \cdot 512$ pixels) are resampled to get images with a lower resolution, e. g. $32 \cdot 32$ pixels. To avoid artifacts, anti-aliasing filters are implemented.

Some parts of the images are shaded by components of the mechanical manipulator. These are detected automatically by evaluating the interference contrast, and theoretical values for the magnitude and the phase are inserted.

The phase shifts introduced in this setup are not very precise due to vibrations of the setup and short time intervals between the acquisition of each image. For this reason a computationally expensive phase calculation algorithm is used [5]. The systematic errors of this method are one order of magnitude lower than those resulting from the well-known standard algorithms [3], if phase shift errors occur.

5.4 Requirements for the phase measurement

It should be emphasized that the tomographic reconstruction algorithms presented above can only handle phase shifts in the projections of no more than π, see section 4, which is equivalent to the difference in optical path length of a half of a wavelength $\frac{\lambda}{2}$. I. e., the phase measurement must achieve a very high accuracy of at least $\frac{\lambda}{100}$, which is attained with the setup [8].

5.5 Immersion fluid

For the measurement of the projection data, the immersion fluid is very important. If its refractive index matches the refractive index n_0 of the unloaded object exactly, the influence of the refractive index of the object on the measured phase is zero, and n_0 can be neglected; see section 2. For a common thickness of the objects of $20\,\mathrm{mm}$, the difference between the refractive indices of the object and the fluid must not exceed $3\cdot10^{-7}$, if a phase of no more than $\frac{\lambda}{100}$ is tolerated due to n_0. A micro dosing system has been built, which allows to prepare the immersion fluid to such a high precision.

An additional problem is the strong temperature dependence of the refractive index of the fluid of approximately $4\cdot10^{-4}/\mathrm{K}$. Thus, the temperature of the immersion fluid must be kept constant during the whole measurement cycle. Only variations of $10^{-3}\,\mathrm{K}$ are allowed to get a maximum phase error of $\frac{\lambda}{100}$.

A controller has been set up [8] to stabilize the temperature of the air of the lab to some $1/100\,\mathrm{K}$, and another to keep the temperature of the immersion fluid constant. Measurements show that the drift of the temperature of the fluid is less than $1/1000\,\mathrm{K}$ for more than an hour.

5.6 Object material and measurement results

To obtain a complete set of projection data, the object is rotated around three axes. For this reason, it can not be loaded during the measurement, but the stress must be resident within the object. The stress is frozen into the photoelastic material by loading the object at a certain high temperature and cooling it off slowly while the load is kept [6]. Photoelastic materials usable for this method are e. g. epoxy (Araldit B) or perspex.

Because the reconstruction algorithms can only handle small amounts of stress resulting in low phase in the projection data, the unloaded object material should be free of residual stress. I. e., an unloaded object should lead to phase images with an overall zero phase.

Test objects were built carefully of epoxy or perspex. They were annealed to reduce the amount of residual stress. Figures 6 a)-d) show the measured phase distribution (modulo 2π) for both positions of the polarizer ($\varphi^{\parallel}$ and $\varphi^{\perp}$) and two different orientations.

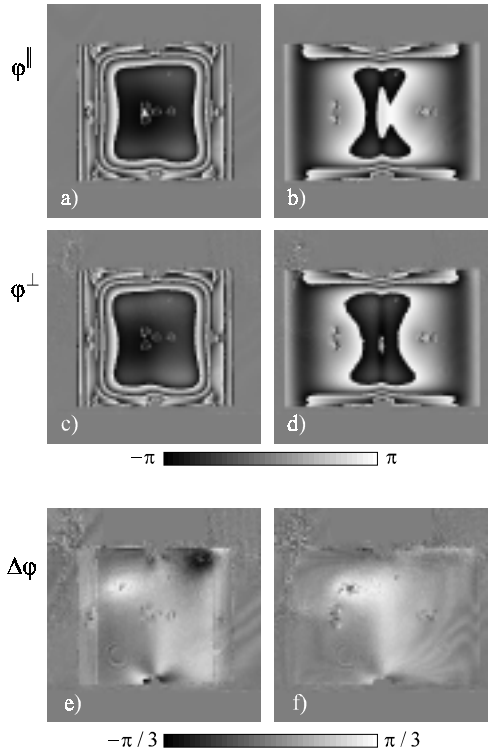

Figure 6: Measured phase distributions (modulo 2π) for two different orientations of an annealed cube of perspex: a),b) polarizer parallel; c),d) polarizer perpendicular; e),f) phase differences (e=c–a ; f=d–b).

It can clearly be seen that the phase shift introduced by the object is not zero, as it should be, and reaches values of much more than π. Two explanations can be given: First, the synthetic materials used for building the objects are hygroscopic. The moisture bound at the surface of the object leads to stress.

The second reason for the non-uniform phase distribution is an inhomogeneous refractive index of the object. During the annealing process, which is associated with heating the material to high temperatures, a change of the chemical properties can take place, and at the surface the refractive index changes.

Because these two effects can not be avoided, the tomographic reconstruction algorithms have to be improved. The principles are described in the following section.

6. IMPROVEMENT OF THE RECONSTRUCTION ALGORITHMS

Figures 6 e) and 6 f) show the phase difference $\varphi^{\perp} - \varphi^{\parallel}$ between both components of the transition matrix. While $\varphi^{\perp}$ and $\varphi^{\parallel}$ show phase values of much greater than π (taking into account the wrapping of the phase), the phase difference no longer shows such high phase values. This raises the hope that there exists a contribution to the phase, which is identical for both components and can be considered separately by the algorithms. For this reason the effect of the components of the stress tensor or the refractive tensor, respectively, on the projections is studied in detail in the following section.

6.1 Contributions to the refractive index field

The stress optical eq. (1) can be generalized to consider the spatial dependence of the refractive index $n_0(\vec{x}) = n_0 + \Delta n_0(\vec{x})$, which can occur for imperfect objects (see previous section):

$$\underline{\underline{n}}(\vec{x}) = n_0(\vec{x}) \cdot \underline{\underline{I}} + A \cdot \mathrm{tr}\left(\underline{\underline{S}}(\vec{x})\right) \cdot \underline{\underline{I}} + B \cdot \underline{\underline{S}}(\vec{x}), \quad (20)$$

and can be reordered to distinguish between terms corresponding to refractive indices and tensorial parts:

$$\underline{\underline{n}}(\vec{x}) = n_L(\vec{x}) \cdot \underline{\underline{I}} + \Delta \underline{\underline{n}}_L(\vec{x}), \quad (21)$$

with

$$n_L(\vec{x}) = \Delta n_0(\vec{x}) + A \cdot \mathrm{tr}\left(\underline{\underline{S}}(\vec{x})\right) + n_{L0}(\vec{x}), \quad (22)$$

$$B \cdot \underline{\underline{S}}(\vec{x}) = n_{L0}(\vec{x}) \cdot \underline{\underline{I}} + \Delta \underline{\underline{n}}_L(\vec{x}), \quad (23)$$

where n_0 has been omitted, since it can be considered during the measurement (see section 5). $n_{L0}(\vec{x})$ can be chosen in such a manner that the magnitude of the components in the main diagonal of $\Delta \underline{\underline{n}}_L(\vec{x})$ is small.

6.2 Partitioning of the projection data

It was shown in the preceding section that the refractive tensor can be split into an isotropic part $n_L(\vec{x}) \cdot \underline{\underline{I}}$ and an anisotropic part $\Delta \underline{\underline{n}}_L(\vec{x})$. It would be helpful, if the effect of the two parts on the projections was separable.

The projections, i. e. the components of the transition matrix, are computed using eqs. (7) and (8). It should be emphasized that the terms in eq. (7) must not be interchanged, because the matrix multiplication of the transition matrices is not commutative. But for the special notation of the refractive tensor, see eq. (21), each transition matrix can be written as:

$$\begin{aligned} \underline{\underline{\Phi}}_{z_{i-1}}^{z_i} &= \mathrm{e}^{-\mathrm{j}k\underline{\underline{n}}^{\perp}(z_i)\Delta z_i} = \mathrm{e}^{-\mathrm{j}k\left(n_L(z_i)\underline{\underline{I}} + \Delta \underline{\underline{n}}_L^{\perp}(z_i)\right)\Delta z_i} \\ &= \mathrm{e}^{-\mathrm{j}kn_L(z_i)\Delta z_i} \cdot \mathrm{e}^{-\mathrm{j}k\Delta \underline{\underline{n}}_L^{\perp}(z_i)\Delta z_i}, \end{aligned} \quad (24)$$

where '$\perp$' means projection of the tensor in the direction of the light wave. Because $\mathrm{e}^{-\mathrm{j}kn_L(z_i)\Delta z_i}$ is only a phase factor, the last product in eq. (24) is commutative.

Thus, eq. (7) can be rearranged by collecting all phase factors in a separate term $\Phi^{\mathrm{iso}}\{n_L\}$, which depends only on the isotropic part of the refractive tensors along the light ray, whereas the tensor $\underline{\underline{\Phi}}^{\mathrm{aniso}}\left\{\Delta \underline{\underline{n}}_L^{\perp}\right\}$ depends on the anisotropic part of the refractive tensors:

$$\underline{\underline{\Phi}}_0^L = \underbrace{\mathrm{e}^{-\mathrm{j}k \sum_{\substack{i=0 \\ m\to\infty}}^{m} n_L(z_i)\Delta z_i}}_{\Phi^{\mathrm{iso}}\{n_L\} = \mathrm{e}^{-\mathrm{j}\varphi^{\mathrm{iso}}}} \cdot \underbrace{\prod_{\substack{i=0 \\ m\to\infty}}^{m} \mathrm{e}^{-\mathrm{j}k\Delta \underline{\underline{n}}_L^{\perp}(z_k)\Delta z_k}}_{\underline{\underline{\Phi}}^{\mathrm{aniso}}\left\{\Delta \underline{\underline{n}}_L^{\perp}\right\}}. \quad (25)$$

6.3 Phase correction of the projections

To decrease the phase values of the projections being processed by the reconstruction algorithms, φ^{iso} should be subtracted from the phase of all components of the corresponding transition matrices. Provided that it would be possible to measure the phase φ^{iso} of Φ^{iso} independently from the anisotropic part, $n_L(\vec{x})$ could be computed by applying well-known tomographic methods (*filtered backprojection* or *ART* [4]), because φ^{iso} can be written as a line integral:

$$\varphi^{\mathrm{iso}} = \int_0^L k n_L(\vec{x}) \mathrm{d}z, \quad (26)$$

for an infinite discretization. To receive the required set of projection data, the object must *only* be rotated *around one axis* [4].

But in practice, only the phase of the components of the transition matrix $\underline{\underline{\Phi}}_0^L$ can be determined by measurements (see section 5). I. e., the measured phase $\varphi^{\parallel}$ is the sum of φ^{iso} and the phase of the (2,2)-element of $\underline{\underline{\Phi}}^{\mathrm{aniso}}$:

$$\varphi^{\parallel} = \varphi^{\mathrm{iso}} + \varphi^{\parallel,\mathrm{aniso}}. \quad (27)$$

The application of a scalar linear tomographic algorithm $S_{\mathrm{lin}}^{-1}\{..\}$ on $\varphi^{\parallel}$, which has been unwrapped [3], leads to the refractive index field:

$$n_{L,\mathrm{rec}}(\vec{x}) = S_{\mathrm{lin}}^{-1}\left\{\varphi^{\parallel}\right\}. \quad (28)$$

Since $\varphi^{\parallel,\mathrm{aniso}}$ depends non-linearly on $\Delta\underline{\underline{n}}(\vec{x})$, $n_{L,\mathrm{rec}}(\vec{x})$ differs from $n_L(\vec{x}) + \left\{\Delta\underline{\underline{n}}_L^{\perp}(\vec{x})\right\}_{(2,2)}$, but the occurring systematic errors are small, because the magnitude of the components of $\Delta\underline{\underline{n}}(\vec{x})$ is low.

Then $n_{L,\mathrm{rec}}(\vec{x})$ is smoothed, yielding $\bar{n}_{L,\mathrm{rec}}(\vec{x})$, on the basis of which phase maps are calculated for each orientation of the object:

$$\varphi_{L,\mathrm{proj}} = \sum_{i=1}^{m} k\bar{n}_{L,\mathrm{rec}}(\vec{x}_i)\Delta z_i \,. \tag{29}$$

All measured components of the transition matrices $\phi^{\parallel/\perp}$ are corrected by the corresponding phase map $\varphi_{L,\mathrm{proj}}$:

$$\phi_{\mathrm{corr}}^{\parallel/\perp} = \phi^{\parallel/\perp} \cdot \mathrm{e}^{\mathrm{j}\varphi_{L,\mathrm{proj}}} \,. \tag{30}$$

The transition matrices $\phi_{\mathrm{corr}}^{\parallel/\perp}$ are the input for the reconstruction algorithms (see section 3). The sum of their result $\underline{\underline{n}}_{\mathrm{rec}}(\vec{x})$ and $\bar{n}_{L,\mathrm{rec}}(\vec{x}) \cdot \underline{\underline{I}}$ is an estimate for the refractive tensor $\underline{\underline{n}}(\vec{x})$ of the object.

In figure 7, the principle of the whole reconstruction process is depicted.

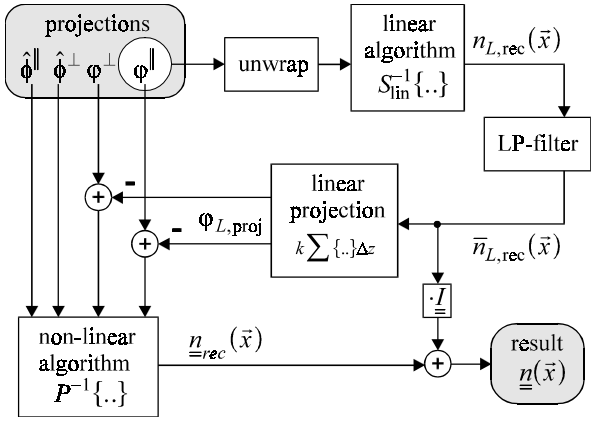

Figure 7: Reconstruction of the stress tensor with phase corrected projections.

6.4 Discussion

A great number of reconstructions have been done with simulated projection data containing high phase values as a results of the described object imperfections. They show good results, even for high values of $\Delta n(\vec{x})$. Thus, a determination of $\underline{\underline{n}}(\vec{x})$ with poor objects should be possible. In addition, the algorithms still converge for higher amounts of stress, if the corrected phase maps are used as input. The enlargement of the area of convergence strongly depends on the material constants A and B. E. g., if perspex is used as object material, the amount of stress may be about ten times greater than in the case of uncorrected phase maps.

Up to now, reconstructions have not been done with experimental data, because the phase unwrapping algorithms have to be improved before they can be applied to measurement data.

7. SUMMARY

The theory of a novel tomographic method for the determination of stress tensor fields has been presented. The method leads to good results for low amounts of stress. An experimental setup for the acquisition of the projection data has been described. Imperfections of the object material require special improvements of the algorithms, which have been presented.

REFERENCES

[1] H. Aben, *"Integrated Photoelasticity",* New York: McGraw-Hill, 1979.

[2] H. Aben, J. Josephson, *"Strange interference blots in the interferometry of inhomogeneous birefringent objects"*, Applied Optics, 1997, **36**, pp. 7172-7179.

[3] K. Creath, *"Phase-measurement interferometry techniques"*, in "Progress in Optics", E. Wolf (ed.), Amsterdam: Elsevier, 1988, pp. 349-393.

[4] A. Kak, M. Slaney, *"Principles of Computerized Tomographic Imaging"*, New York: IEEE Press, 1988.

[5] S. Kim, M. Kang, G. Han, *"Accelerated phase-measuring algorithm of least squares for phase-shifting interferometry"*, Optical Engineering, 1997, **36**, pp. 3101-3106.

[6] C. Rohrbach (ed.), *"Handbuch für experimentelle Spannungsanalyse"*, Düsseldorf: VDI-Verlag, 1989.

[7] D. Schupp, *"Determination of 3-D stress by optical tensor field tomography"*, Proc. SPIE, Vol. 3098, 1997, pp. 431-441.

[8] D. Schupp, *"Optische Tensortomographie zur Bestimmung räumlicher Spannungsverteilungen"*, tm-Technisches Messen, München: Oldenbourg, to be published.

[9] P.S. Theocaris, E.E. Gdoutos, *"Matrix Theory of Photoelasticity"*, Berlin: Springer, 1979.

[10] R.Y. Tsai, *"A Versatile Camera Calibration Technique for High-Accuracy 3D Machine Vision Metrology Using Off-the-Shelf TV Cameras and Lenses"*, IEEE: Journal of Robotics and Automation, Vol. RA-3, No. 4, 1987, pp. 323-344.